symmetry

MDPI

Article

Visualization of the Preacceleration Process for High-Harmonic Generation in Solids

Fangyan Gao [1], Yonglin He [1,2,3], Lingyu Zhang [1], Shengpeng Zhou [1] and Jing Guo [1,*]

[1] Institute of Atomic and Molecular Physics, Jilin University, Changchun 130012, China; gaofy20@mails.jlu.edu.cn (F.G.); hyl@hxu.edu.cn (Y.H.); zhanglingy21@mails.jlu.edu.cn (L.Z.); spzhou@jlu.edu.cn (S.Z.)
[2] School of Physics and Electromechanical Engineering, Hexi University, Zhangye 734000, China
[3] Institute of Theoretical Physics, Hexi University, Zhangye 734000, China
* Correspondence: gjing@jlu.edu.cn

Abstract: The high-order harmonic generation (HHG) in ZnO is investigated by numerically solving semiconductor Bloch equations (SBEs), which can be explained well by a four-step model. In this model, preacceleration is the first step, in which the electron is accelerated in the valence band until it reaches the point of the minimum band gap. To prove the existence of the preacceleration process, SBE-based **k** -resolved harmonic spectra and the transient conduction-band population are presented. The results show that the contribution of crystal-momentum channels away from the minimum band gap via preacceleration is non-negligible. Furthermore, the X-shaped distribution in the **k**-resolved spectra can be described well by the preacceleration process. Based on the above analysis, we can conclude that the preacceleration process plays an important role in HHG.

Keywords: high-order harmonic generation; preacceleration process; crystal-momentum-resolved spectrum; recollision model in solid

Citation: Gao, F.; He, Y.; Zhang, L.; Zhou, S.; Guo, J. Visualization of the Preacceleration Process for High-Harmonic Generation in Solids. *Symmetry* **2022**, *14*, 1281. https://doi.org/10.3390/sym14071281

Academic Editor: Jacek Karwowski

Received: 17 May 2022
Accepted: 7 June 2022
Published: 21 June 2022

1. Introduction

With the development of laser technology, the interaction between lasers and atoms or molecules has become a hot topic in strong-field physics, which includes lots of nonlinear phenomena, and high-order harmonic generation (HHG) has attracted extensive great attention [1–5]. In 1987, Shore and Knight theoretically predicted the existence of high-order harmonics [6]. In the same year, Mcpherson et al. [7] experimentally observed HHG in noble gases for the first time. The harmonic spectrum has the following characteristics: low-perturbation regime at low orders, plateau for intermediate orders, and cutoff at high orders [8]. However, the appearance of higher harmonics in the plateau region and the cutoff region cannot be explained by the perturbative theory. In 1993, Corkum et al. proposed a "semiclassical three-step model" [4]: (1) in an intense laser field, one side of the Coulomb potential is pushed down, and the electron tunnels through the barrier; (2) the ionized electron is accelerated away from the atoms or molecules by laser fields; (3) under some conditions, the electron returns to the core to recombine with the parent ion and emits a high-energy photon. This model gives a clear physical picture of HHG. In the past few decades, a large number of studies have clarified the physical mechanism of gas-phase HHG [1,9].

High-order harmonics can be generated in solids [10–12], plasma [13], and liquids [14–16] driven by intense ultrafast lasers. For example, Bian et al. [17] investigated liquid-phase HHG theoretically by using a disordered linear chain. In 2011, Ghimire et al. [18] observed non-perturbative HHG in solids clearly for the first time, and HHG in solids has also attracted considerable attention [18–21]. For example, Lu et al. [22] investigated HHG in strongly correlated systems under strong laser irradiation by employing the exact diagonalization method. HHG in solids not only provides a new way to obtain

high-intensity XUV light but also opens the door of attosecond physics in condensed matter [23–26]. However, until now, HHG in solids has exhibited many unique and unexplored characteristics [27–29], and the underlying physics of HHG in solids has not been fully understood. At present, it is widely accepted that HHG in solids comes from two major contributions: intraband current and interband polarization [30–32]; the complex coupling between the two mechanisms not only affects the charge injection from the valence band to the conduction band but also affects the motion of excited-state electron wave packets in momentum space [33–40].

In 2019, Lu et al. [41] proposed a four-step model to investigate HHG in solids driven by circularly and elliptically polarized laser fields. In the four-step model, these electrons are firstly accelerated in the valence band, known as the preacceleration process. Second, tunneling excitation occurs when the electrons reach the point of the minimum band gap. Third, after ionization, the hole in the valence band and the electron in the conduction band are accelerated in opposite directions that obey the acceleration theorem. During the acceleration process, the instantaneous energy difference between the electron and the hole is expressed as $\triangle\ E(\mathbf{K}(t)) = E_c(\mathbf{K}(t)) - E_v(\mathbf{K}(t))$, where E_c and E_v represent the energy bands of the conduction band and valence band. Fourth, when the electron and hole are driven back towards their initial position and eventually recollide with each other, they emit momentary band-gap energy as a photon. The main difference between the three-step recollision model in real space and the four-step model is that the preacceleration process is included in the four-step model. Later, there have also been many studies on the harmonic spectrum considering the crystal-momentum resolution of the preacceleration process [42–46]. The preacceleration process clearly claims that the valence-band electrons in the entire first Brillouin zone must be taken into account in solid HHG simulations.

The main motivation of this work is to explore the contribution of the preacceleration process to HHG in solids. This paper is organized as follows: In Section 2, we introduce the two-band semiconductor Bloch equations (SBEs) used in this paper. Our numerical simulation results are presented and discussed in Section 3. Our main results are summarized in Section 4. Atomic units are used throughout this paper unless otherwise indicated.

2. Theoretical Methods

HHG in solids is modeled by two-band SBEs, which includes coupled interband and intraband dynamics [19,30,47–49]:

$$\dot{n}_m(\mathbf{K},t) = i\sum_{m\neq m'}\Omega_{mm'}\pi_{mm'}\exp[iS_{mm'}(\mathbf{K},t)] + c.c. \tag{1}$$

$$\begin{aligned}\dot{\pi}_{mm'}(\mathbf{K},t) &= -\frac{\pi_{mm'}(\mathbf{K},t)}{T_2} + i\Omega^*_{mm'}(n_m - n'_m)\exp[iS_{mm'}(\mathbf{K},t)]\\ &+i\sum_{m''\notin m,m'}(\Omega_{m'm''}\pi_{m'm''}\exp[iS_{m'm''}] - \Omega^*_{m'm''}\pi^*_{m'm''}\exp[-iS_{m'm''}])\end{aligned} \tag{2}$$

where $\pi_{mm'}$ is the density matrix element, representing the quantum coherence between the two bands; n_m is population of the valance band ($m = v$) and the conduction band ($m = c$); $\Omega_{mm'}(\mathbf{K},t) = \mathbf{F}(t)\cdot d(\mathbf{K}+\mathbf{A}(t))$ is the Rabi frequency; d(**k**) represents the transition dipole moment between the two bands [50]; $S_{mm'}(\mathbf{K},t) = \int_{-\infty}^{t}\varepsilon_{mm'}(\mathbf{K}+\mathbf{A}(t'))dt'$ is the classical action; and $\varepsilon_{mm'} = E_m - E_{m'}$ is the **k**-dependent transition energy between the valence band and the conduction band.

T_2 is a dephasing-time term describing the coherence between the electron and hole [51–53]. According to Bloch's acceleration theorem [54], the crystal momentum of an electron within a given band changes according to $\mathbf{K}(t) = \mathbf{k} - \mathbf{A}(t)$ [19], where $\mathbf{A}(t)$ is the vector potential of the electric field and **k** is the initial momentum. The polarization associated with $\pi_{mm'}(\mathbf{k},t)$ is defined as [19]:

$$\mathbf{p}_{mm'}(\mathbf{K},t) = d_{mm'}(\mathbf{K}+\mathbf{A}(t))\pi_{mm'}(\mathbf{K},t)\exp[iS_{mm'}(\mathbf{K},t)] + c.c. \tag{3}$$

where $\mathbf{p}_{mm'}(\mathbf{K},t)$ represents the polarizability of the two bands. Intraband current $\mathbf{j}_{ra}(t)$ and interband current $\mathbf{j}_{er}(t)$ can be written as follows [19]:

$$\mathbf{j}_{ra}(t) = \sum_{m=c,v} \int_{BZ} \mathbf{v}_m[\mathbf{K}+\mathbf{A}(t)] n_m(\mathbf{K},t) d^3\mathbf{K} \tag{4}$$

$$\mathbf{j}_{er}(t) = \frac{d}{dt} \sum_{m\neq m'} \int_{BZ} \mathbf{p}_{mm'}(\mathbf{K},t) d^3\mathbf{K} \tag{5}$$

where $\mathbf{v}_m[\mathbf{k}] = \nabla_{\mathbf{k}} E_m[\mathbf{k}]$ is the gradient of the dispersion relation, called the group velocity of the electron (hole) in the conduction band (valence band). The interband and intraband high-order harmonic spectra are calculated by the modulus square of the Fourier transform (FT) of the time derivatives of $\mathbf{j}_{ra}(t)$ and $\mathbf{j}_{er}(t)$ [51]:

$$\mathbf{I}_{HHG_{jra}} = \omega^2 |\mathcal{F}_T\{\mathbf{j}_{ra}(t)\}|^2 \tag{6}$$

$$\mathbf{I}_{HHG_{jer}} = \omega^2 |\ \mathcal{F}_T\{\mathbf{j}_{er}(t)\}\ |^2 \tag{7}$$

The total high-order harmonic spectrum is written as:

$$\mathbf{I}_{HHG_{total}} = \omega^2 |\mathcal{F}_T\{\mathbf{j}_{ra}(t) + \mathbf{j}_{er}(t)\}|^2 \tag{8}$$

In our one-dimensional (1D) SBE simulation, the linearly polarized laser field with Gaussian envelope is given by:

$$F(t) = F_0 \exp[-2\ln(2)(\frac{t}{\tau})^2] \cos(\omega_0 t + \phi) \tag{9}$$

where F_0 is the peak of the electric field inside the crystal; ω_0 is the circular frequency of the fundamental laser; and ϕ is the carrier–envelope phase. For a ZnO crystal, the electric field is linearly polarized along the $\Gamma - M$ direction of the Brillouin zone. The selection of laser intensity makes the excitation of the high conduction band negligible, so the two-band model is reasonable and can be adopted.

3. Results and Discussion

From Figure 1a we can see the crystal structure of wurtzite ZnO, which has the hexagonal symmetry. The first Brillouin zone of wurtzite ZnO crystals and the associated high-symmetric points Γ, K, and M are shown in Figure 1b. The wurtzite ZnO is a typical direct band-gap semiconductor, and the lattice constants are $a = 3.2493$, $b = 3.2493$, and $c = 5.2054$. The structure parameters for calculating the bands of a model ZnO crystal are taken from Ref. [48].

The high-order harmonic spectra of ZnO driven by linearly polarized laser fields with field strength $F_0 = 0.004$ (corresponding to the vacuum field intensity of $I = 5.5 \times 10^{11}$ W/cm^2) are shown in Figure 2. We chose $\tau = 6$ optical cycles, $\phi = 0$, and a total pulse duration of 25 optical cycles, where $\omega_0 = 0.014$, $T_2 = \frac{T_0}{4}$, and $\lambda = 3250$ nm. The spectra of the two currents present a platform from the 9th harmonic order to the 29th (both orders are marked with black short-dashed–dotted lines). As shown in Figure 2, the harmonic spectra in the plateau regime are dominated by interband polarization with the laser parameters we used.

To understand the physical mechanism of HHG in solids, it is useful to describe the motion of electron–hole pairs by the three-step recollision model in real space [18,19,24]: (1) Near the peak of the electric field, a small portion of electrons near the minimum band gap in the valence band vertically tunnel to the lowest conduction band, leaving a hole in the valence band (tunneling excitation process). (2) Then, the electron–hole pair accelerates in the bands under the action of an electric field (intraband acceleration process). (3) The electron recombines with the hole and emits a harmonic photon with energy given

by the energy difference between the conduction and the valence bands (electron–hole recombination process).

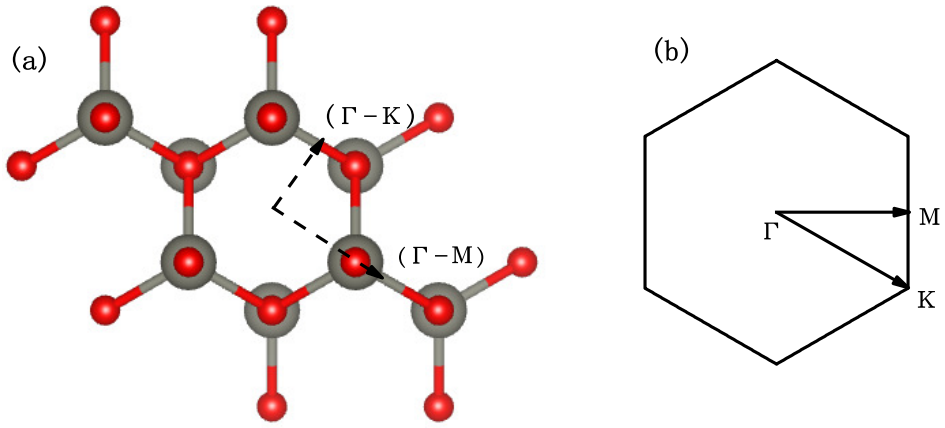

Figure 1. (**a**) Top view of wurtzite structure in ZnO crystal, with O and Zn atoms being represented by red and gray spheres, respectively. (**b**) The first Brillouin zone in the reciprocal lattice, where Γ, *K*, and *M* are the high symmetry points.

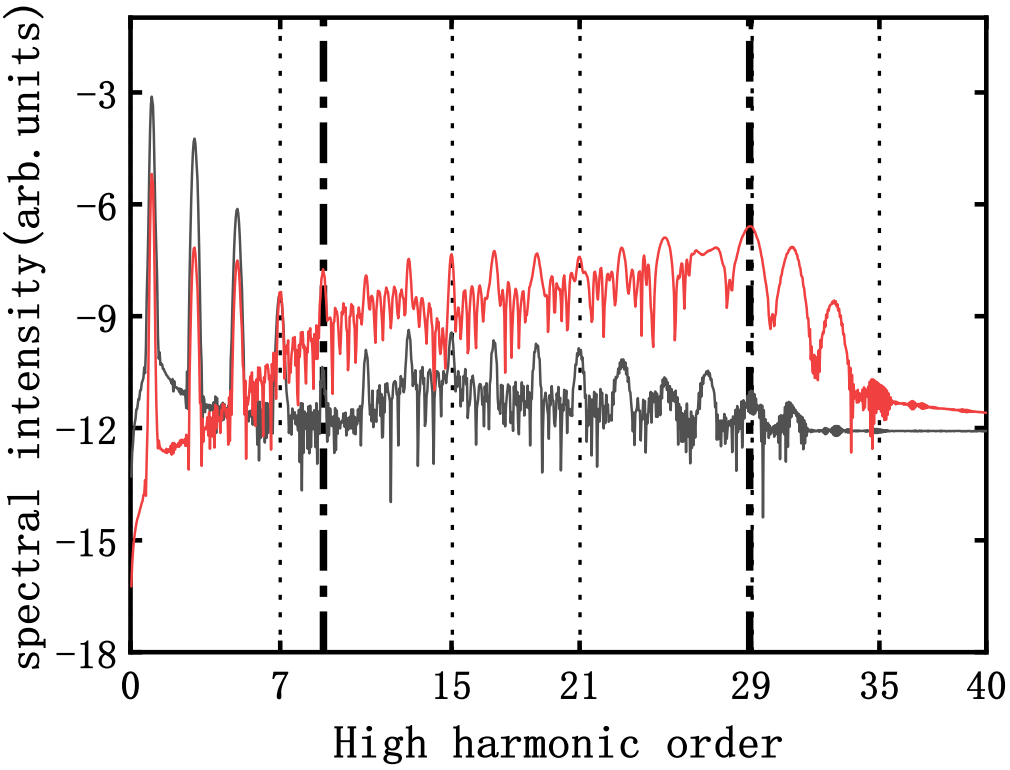

Figure 2. Harmonic spectra of ZnO with $F_0 = 0.004$ and $\lambda = 3250$ nm. The black solid line and the red solid line indicate intraband and interband harmonics, respectively. The black short-dashed–dotted lines indicate the position of the minimum band gap and the cutoff of the harmonic spectrum.

As predicted by the three-step recollision model, Figure 3a shows the recollision energies of the electron and hole as functions of tunneling and recollision time in ZnO crystals. The trajectories with earlier ionization time and later recollision time are called long trajectories. On the contrary, the short trajectories have a later ionization time and earlier recollision time [55]. Figure 3b shows the long and short trajectories of the 17th harmonic in real space with different ionization time in ZnO crystals. The green lines represent the electron displacement (solid line) and hole displacement (dashed line) with

the ionization time of −0.474 optical cycles, corresponding to the long trajectory indicated by the green arrow in Figure 3a, and the corresponding recollision time of 0.408 optical cycles represented by the green arrow in Figure 3b. In Figure 3b, the blue lines represent the electron displacement (solid line) and hole displacement (dashed line) with the ionization time of −0.35 optical cycles, corresponding to the short trajectory indicated by the blue arrow in Figure 3a, and the corresponding recollision time of −0.023 optical cycles represented by the blue arrow in Figure 3b. From Figure 3, the long and the short trajectories can be intuitively distinguished.

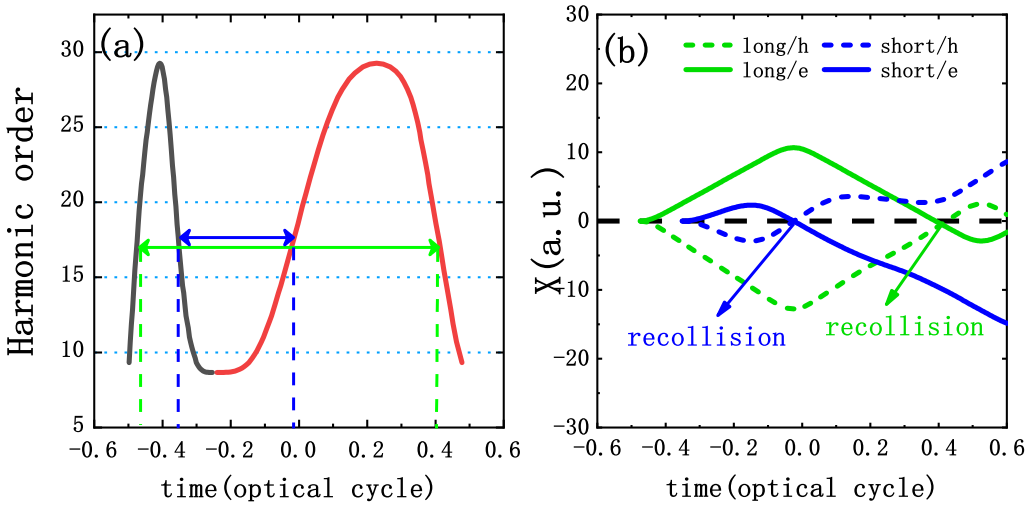

Figure 3. (**a**) The energy of the recollision in a ZnO crystal varies with tunneling ionization (black solid line) and recollision time (red solid line). (**b**) The short trajectories of the electron (blue solid line) and the hole (blue dotted line) for the 17th harmonic and the long trajectories of the electron (green solid line) and the hole (green dotted line). The parameters are the same as those in Figure 2.

The above recollision model for solids is different from that for atoms. Firstly, in atoms, only electrons move under the drive of the laser field. However, in solids, both electrons and holes move under the drive of the laser field, and at a certain time, the electron and hole recombine with each other and emit photons, i.e., HHG. Secondly, the ionized electron of an atom can be viewed as a free electron accelerated by a laser field. In solids, the ionized electron is in the periodic potential field of the crystal, and the trajectories of electrons and holes depend on the band structure of the solid. Finally, the kinetic energy of the electrons of an atom is related to the ionization potential of the atom and the laser intensity, while the maximum harmonic energy in solids is limited to the band-gap energy.

Figure 4a presents the time–frequency distribution of the total harmonic spectra of the Γ channel. Figure 4b presents the time–frequency distribution of the total harmonic spectra of the whole channel in the Brillouin zone. From Figure 4a,b, we find that there is a big difference between the two time–frequency distributions. This shows that except for the Γ channel, the contribution of other channels cannot be ignored. Next, we need to study the mechanism for the contribution of other channels to the harmonic spectrum.

In solids, when the driving field is added, the electrons at the Γ point are tunneled vertically to the conduction band. With the increase in the intensity of the driving field, more and more electrons are excited to the conduction band. We study the dynamics of multiple crystal-momentum channels formed by the electrons excited to the conduction band in the linearly polarized laser fields by comparing the absence and the existence of the preacceleration process in Figures 5 and 6.

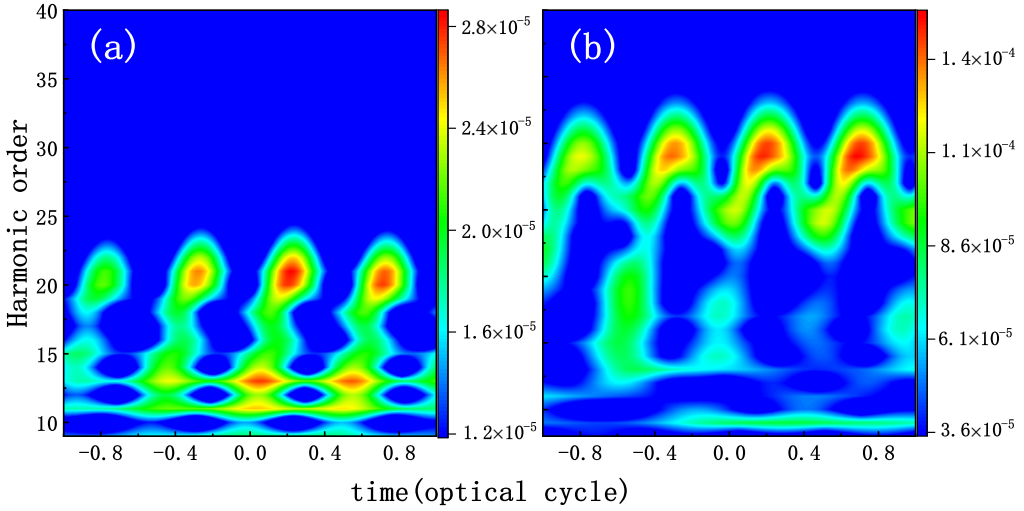

Figure 4. The time–frequency analysis of the total harmonic spectra of a ZnO crystal with logarithmic color scale. The laser parameters are the same as those in Figure 2.

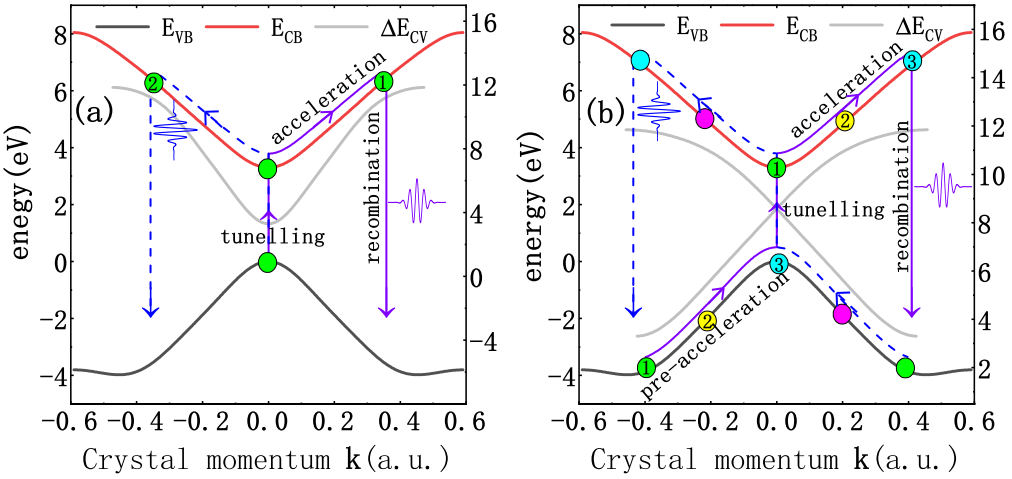

Figure 5. (**a**) Schematic diagram of **k**-space dynamics without preacceleration process. Curves with arrows show the electron tunneling from the valence band to the conduction band, acceleration within the conduction band, and interband recombination, respectively. (**b**) Schematic diagram of **k**-space dynamics with preacceleration process. Curves with arrows represent the preacceleration process in the valence band, tunneling from the valence band to the conduction band, intraband acceleration process, and interband recombination, respectively. The colored circles represent electrons belonging to different momentum channels. Black and red curves in (**a**,**b**) represent the valence band and conduction band of ZnO crystals, respectively. The gray curves represent the energy difference between the conduction band and the valence band.

According to the Landau–Zener tunneling theory [56], tunneling has an exponential dependence on the band gap. Tunneling ionization mainly occurs at the minimum band gap (Γ point, $\mathbf{k}_0 = 0$); therefore, it gives the largest contribution to HHG, and the tunneling ionization at other **k** channels can be reasonably ignored. This is not to say that the contribution of other **k** channels is small, but that tunneling ionization mainly occurs at the minimum band gap. The contributions of other **k** channels are also very important due to the so-called preacceleration process. An electron initially located at $\mathbf{k} \neq 0$ in the valence band is firstly accelerated in the valence band before tunneling ionization, and tunneling ionization occurs when the electron reaches the Γ point.

Figure 5a shows the **k**-space dynamics without preacceleration process. In the presence of the laser field, the instantaneous crystal momentum of the electron is $\mathbf{K}(t) = \mathbf{k}_0 + \mathbf{A}(t)$. Here, $\mathbf{k}_0$ is the initial crystal momentum of the electron, and $\mathbf{A}(t)$ is the vector potential of the laser. An electron preferentially enters the conduction band at the Γ point ($\mathbf{k}_0 = 0$) and subsequently moves in the conduction band governed by the acceleration theorem. Interband harmonics might be emitted at any time during the acceleration process in the conduction band, and the photon energy is given by the band gap at the instantaneous crystal momentum, $\mathbf{K}(t)$. Therefore, we should obtain a V-shaped distribution in the **k**-resolved spectra as shown by the gray curve in Figure 5a.

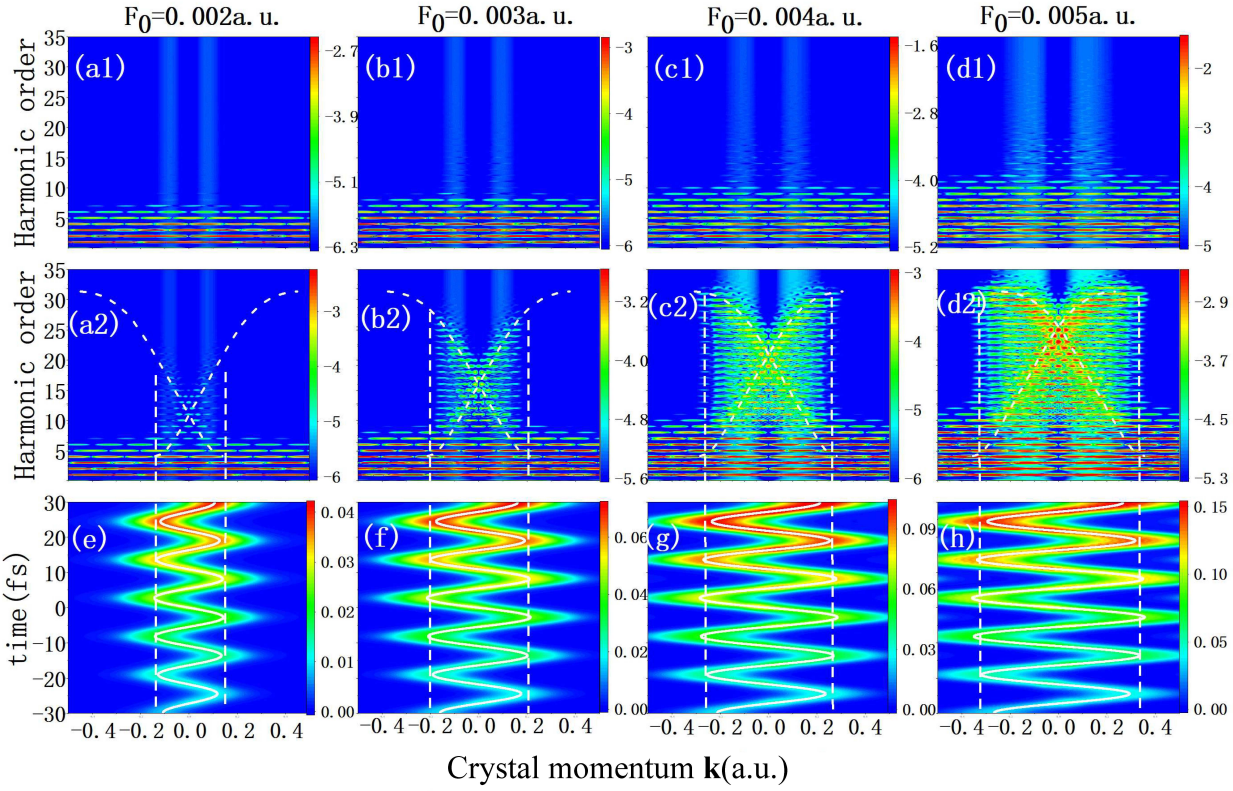

Figure 6. **k**-resolved profile of HHG from ZnO driven by linearly polarized laser pulse. **k**-resolved intraband (**a1**–**d1**) and total harmonic spectra (**a2**–**d2**) as functions of crystal momentum **k**. (**e**–**h**) Time-dependent conduction-band population in the moving **K**-space frame. The white solid lines represent $\mathbf{A}(t)$, and the white dotted lines indicate $\pm\mathbf{A}_{max}(t)$. Panels (**a1**–**h**) are given on the same logarithmic scale, and (**a1**–**d1**), (**a2**–**d2**), and (**e**–**h**) correspond to the field strengths of the driving laser field of 0.002, 0.003, 0.004, and 0.005.

What characteristics would the **k**-resolved spectra have if the preacceleration process existed? Figure 5b shows the **k**-space dynamics with preacceleration process. Let us consider the case of electrons initially located at different **k** channels, e.g., $\mathbf{k}_0 = -0.4, -0.2$, and 0 for the 1st, 2nd, and 3rd electrons in the valence band of Figure 5b; we assume that the peak of vector potential $\mathbf{A}_{max}$ equals 0.4.

The motion of the 1st electron can be described by the following steps: Firstly, the 1st electron experiences the intraband preacceleration before tunneling ionization. The maximum momentum obtained by the 1st electron is $\mathbf{K}_{max} = \mathbf{k}_0 + \mathbf{A}_{max} = 0$. Secondly, the 1st electron is excited from the valence band to the conduction band by tunneling at the minimum band gap ($\mathbf{k}_0 = 0$). Finally, the recombination process also occurs at $\mathbf{k} = 0$. Therefore, due to the fact that the 1st electron cannot gain additional momentum, the photon energy of the harmonic contributed by the $\mathbf{k}_0 = 0.4$ channel equals the band-gap energy at the Γ point ($\mathbf{k} = \mathbf{K}_{max} = 0$).

The motion of the 2nd electron can be described by the following steps: Firstly, the 2nd electron experiences the same intraband preacceleration as the 1st electron. Secondly, tunneling ionization occurs when the 2nd electron reaches the Γ point ($\mathbf{k} = 0$). Thirdly, due to the fact that ($\mathbf{K}_{max}$) equals 0.2 for this case, the 2nd electron undergoes additional intraband acceleration in the conduction band, and the interband harmonic is emitted during the intraband acceleration process in the conduction band. Finally, the maximum photon energy of the harmonic contributed by the 2nd electron equals the band-gap energy at $\mathbf{k} = \mathbf{K}_{max} = 0.2$.

For the same reason, the maximum photon energy of the harmonic contributed by the 3rd electron equals the band-gap energy at $\mathbf{k} = \mathbf{K}_{max} = 0.4$. The electron dynamics for momentum channels with $\mathbf{k} > 0$ are similar to those for the above momentum channels with $\mathbf{k} < 0$.

Based on the above analysis, the maximum photon energy of the harmonics contributed by different **k** channels can be obtained by translating the gray curve in Figure 5a to the left or right by $\mathbf{A}_{max}$. Therefore, an X-shaped distribution in the **k**-resolved spectra should be obtained as shown by the gray curve in Figure 5b.

To prove the existence of the preacceleration process, the SBE-based **k**-resolved harmonic spectra are presented. In order to see the contribution of different **k** channels intuitively, we obtain the **k**-resolved intrabands (Figure 6a1–d1) and total harmonic spectra (Figure 6a2–d2) at different laser intensities as well as the time-dependent population in the conduction band as functions of momentum $\mathbf{K}(t)$ (Figure 6e–h) in Figure 6.

Figure 6a1–d1 present the intraband harmonic spectra as functions of crystal momentum **k** under different laser intensities. It is found that when $F_0 = 0.002$, the cutoff of the intraband harmonic reaches the 5th order, and when $F_0 = 0.005$, the cutoff of the intraband harmonic reaches the 10th order. Therefore, Figure 6a1–d1 indicate that the order of the intraband harmonics is also extended with F_0.

Figure 6a2–d2 present the total harmonic spectra as functions of crystal momentum **k** under different laser intensities. When $F_0 = 0.002$, it is observed in Figure 6e that the peak of vector potential $\mathbf{A}_{max}$ equals about 0.15. In Figure 6a2, the electron dynamics for the momentum channel with the $\mathbf{k}_0 = -0.15$ channel are similar to those of the 1st electron shown in Figure 5b. The maximum photon energy of the harmonics contributed by different **k** channels can be obtained by translating the gray curve in Figure 5a to the left or right by $\mathbf{A}_{max} = 0.15$, i.e., the white dashed line in Figure 6a2. The range of the crystal momentum of the corresponding **k**-resolved HHG spectra is approximately $[-0.15, 0.15]$.

When $F_0 = 0.003, 0.004$, and 0.005, it is observed in Figure 6f–h that the peaks of vector potential $\mathbf{A}_{max}$ equal about 0.21, 0.29, and 0.36. In Figure 6b2–d2, the maximum photon energy of the harmonics contributed by different **k** channels equals the band-gap energy at $\mathbf{k} = \mathbf{K}_{max} = 0.21, 0.29$, and 0.36. The analysis of electrons in other **k** channels in Figure 6b2–d2 is similar to that of Figure 5b. The white dashed lines in Figure 6b2–d2 can be obtained by translating the gray curve in Figure 5a to the left or right by $\mathbf{A}_{max} = 0.21, 0.29$, and 0.36, respectively. The ranges of the crystal momentum of the corresponding **k**-resolved harmonics are determined to be $[-0.21, 0.21]$, $[-0.29, 0.29]$, and $[-0.36, 0.36]$, respectively. From Figure 6b2–d2, we also find that the X-shaped distributions in the **k**-resolved spectra are in good agreement with the white dashed lines predicted by the preacceleration process. In Figure 6a2–d2, it is found that with the increase in F_0, the width of the distribution of **k**-resolved spectra gradually increases, and the cutoff energy of the total harmonic spectra also increases.

Figure 6e–h present the time-dependent population of electrons in the conduction band as functions of moving momentum $\mathbf{K}(t)$, with the white solid lines representing $\mathbf{A}_{max}$. The electrons are excited to the conduction band and move in the conduction band with the laser field. In Figure 6e, when $F_0 = 0.002$, the range of the instantaneous population of the electrons in the conduction band is consistent with that of the vector potential, i.e., $\pm\mathbf{K}_{max} = \pm\mathbf{A}_{max} = \pm 0.15$. Since the farthest position of the acceleration of the electrons in the conduction band is determined by instantaneous crystal momentum

$\mathbf{K}_{max} = \mathbf{k}_0 + \mathbf{A}_{max}$, the instantaneous population of the electrons represents the dynamics of the electron at the Γ point, similar to the 3rd electron in Figure 5b. The area with white dotted lines indicates the range of electronic acceleration in the conduction band under the laser parameter, i.e., [−0.15, 0.15], which is consistent with the range of crystal momentum in Figure 6a2 and also proves the preacceleration process. For the same reason, in Figure 6f–h, when the peak values of the vector potential are equal to 0.21, 0.29, and 0.36, the areas with white dotted lines represent the ranges of the acceleration of the electron in the conduction band, respectively, i.e., [−0.21, 0.21], [−0.29, 0.29], and [−0.36, 0.36], which correspond to the ranges of the crystal momentum in Figure 6b2–d2, respectively. In Figure 6e, at $F_0 = 0.002$, the peak of vector potential $\mathbf{A}_{max}$ equals about 0.15. According to the acceleration theorem, the farthest positions that the electron at the Γ point can reach are $\mathbf{K}_{max}(t) = \pm\mathbf{A}_{max}(t) = \pm 0.15$. When the laser intensity increases, as shown by the white dotted line in Figure 6e–h, the corresponding farthest positions of the electron are $\mathbf{K}_{max}(t) = \pm 0.21$, $\mathbf{K}_{max}(t) = \pm 0.29$, and $\mathbf{K}_{max}(t) = \pm 0.36$, respectively. This is confirmed by the transient population of the conduction band obtained by SBE simulations. It is clear in Figure 6e–h that with the increase in laser intensities, the probability of electrons tunneling to the conduction band increases, so the instantaneous population of electrons in the conduction band also increases. Based on the above analysis, we conclude that the preacceleration process plays an important role in HHG, and our results also verify the four-step model for HHG in solids.

4. Conclusions

In summary, we theoretically investigate HHG in ZnO crystals by linearly polarized laser pulses. We explain the X-shape distribution of HHG by a preacceleration process. In the four-step model, these electrons are firstly accelerated in the valence band, known as the preacceleration process. Second, tunneling excitation occurs when the electrons reach the point of the minimum band gap. Third, after ionization, the hole in the valence band and the electron in the conduction band are accelerated in opposite directions that obey the acceleration theorem. During the acceleration process, the instantaneous energy difference between the electron and the hole is expressed as $\triangle\ E(\mathbf{K}(t)) = E_c(\mathbf{K}(t)) - E_v(\mathbf{K}(t))$, where E_c and E_v represent the energy bands of the conduction band and the valence band. Fourth, when the electron and hole are driven back towards their initial position and eventually recollide with each other, they emit momentary band-gap energy as a photon. The preacceleration process for HHG in solids is visualized by the crystal-momentum-resolved harmonic spectra and the transient conduction-band population, which confirm the four-step model for HHG in solids. Thus, except for the Γ channel, other channels in the first Brillouin zone also play important roles in the preacceleration process.

Author Contributions: Conceptualization, F.G.; methodology, F.G. and Y.H.; software, F.G. and Y.H.; resources, Y.H. and J.G.; data curation, F.G.; writing—original draft, F.G.; writing—review and editing, Y.H. and J.G.; supervision, L.Z., Y.H., S.Z. and J.G. All authors have read and agreed to the published version of the manuscript.

Funding: This research study was supported by National Natural Science Foundation of China (grants No. 12074146, No. 11974007, No. 11964008, and No. 11464010).

Institutional Review Board Statement: Not applicable.

Informed Consent Statement: Not applicable

Data Availability Statement: The data presented in this study are available upon request from the corresponding author.

Conflicts of Interest: The authors declare no conflict of interest.

References

1. Krausz, F.; Ivanov, M. Attosecond physics. *Rev. Mod. Phys.* **2009**, *81*, 163–234. [CrossRef]
2. Lan, P.; Ruhmann, M.; He, L.; Zhai, C.; Wang, F.; Zhu, X.; Zhang, Q.; Zhou, Y.; Li, M.; Lein, M.; et al. Attosecond Probing of Nuclear Dynamics with Trajectory-Resolved High-Harmonic Spectroscopy. *Phys. Rev. Lett.* **2017**, *119*, 033201. [CrossRef] [PubMed]
3. He, L.; Lan, P.; Le, A.T.; Wang, B.; Wang, B.; Zhu, X.; Lu, P.; Lin, C.D. Real-Time Observation of Molecular Spinning with Angular High-Harmonic Spectroscopy. *Phys. Rev. Lett.* **2018**, *121*, 163201. [CrossRef] [PubMed]
4. Corkum, P.B. Plasma perspective on strong field multiphoton ionization. *Phys. Rev. Lett.* **1993**, *71*, 1994–1997. [CrossRef]
5. Li, Y.; Sato, T.; Ishikawa, K.L. High-order harmonic generation enhanced by laser-induced electron recollision. *Phys. Rev. A* **2019**, *99*, 043401. [CrossRef]
6. Shore, B.W.; Knight, P.L. Enhancement of high optical harmonics by excess-photon ionisation. *J. Phys. B At. Mol. Phys.* **1987**, *20*, 413–423. [CrossRef]
7. McPherson, A.; Gibson, G.; Jara, H.; Johann, U.; Luk, T.S.; McIntyre, I.A.; Boyer, K.; Rhodes, C.K. Studies of multiphoton production of vacuum-ultraviolet radiation in the rare gases. *J. Opt. Soc. Am. B* **1987**, *4*, 595–601. [CrossRef]
8. Winterfeldt, C.; Spielmann, C.; Gerber, G. Colloquium: Optimal control of high-harmonic generation. *Rev. Mod. Phys.* **2008**, *80*, 117–140. [CrossRef]
9. Le, A.T.; Lucchese, R.R.; Tonzani, S.; Morishita, T.; Lin, C.D. Quantitative rescattering theory for high-order harmonic generation from molecules. *Phys. Rev. A* **2009**, *80*, 013401. [CrossRef]
10. Faisal, F.H.M.; Kamiński, J.Z. Floquet-Bloch theory of high-harmonic generation in periodic structures. *Phys. Rev. A* **1997**, *56*, 748–762. [CrossRef]
11. Pronin, K.A.; Bandrauk, A.D.; Ovchinnikov, A.A. Harmonic generation by a one-dimensional conductor: Exact results. *Phys. Rev. B* **1994**, *50*, 3473–3476. [CrossRef] [PubMed]
12. He, Y.L.; Guo, J.; Gao, F.Y.; Liu, X.S. Dynamical symmetry and valley-selective circularly polarized high-harmonic generation in monolayer molybdenum disulfide. *Phys. Rev. B* **2022**, *105*, 024305. PRB, [CrossRef]
13. Thaury, C.; Quéré, F. High-order harmonic and attosecond pulse generation on plasma mirrors: Basic mechanisms. *J. Phys. B At. Mol. Opt. Phys.* **2010**, *43*, 213001. [CrossRef]
14. Xia, C.L.; Li, Z.L.; Liu, J.Q.; Zeng, A.W.; Lü, L.J.; Bian, X.B. Role of charge-resonance states in liquid high-order harmonic generation. *Phys. Rev. A* **2022**, *105*, 013115. [CrossRef]
15. DiChiara, A.D.; Sistrunk, E.; Miller, T.A.; Agostini, P.; DiMauro, L.F. An investigation of harmonic generation in liquid media with a mid-infrared laser. *Optics Express* **2009**, *17*, 20959–20965. [CrossRef]
16. Luu, T.T.; Yin, Z.; Jain, A.; Gaumnitz, T.; Pertot, Y.; Ma, J.; Wörner, H.J. Extreme–ultraviolet high–harmonic generation in liquids. *Nat. Commun.* **2018**, *9*, 3723. [CrossRef]
17. Zeng, A.W.; Bian, X.B. Impact of Statistical Fluctuations on High Harmonic Generation in Liquids. *Phys. Rev. Lett.* **2020**, *124*, 203901. [CrossRef]
18. Ghimire, S.; DiChiara, A.D.; Sistrunk, E.; Agostini, P.; DiMauro, L.F.; Reis, D.A. Observation of high-order harmonic generation in a bulk crystal. *Nat. Phys.* **2011**, *7*, 138–141. [CrossRef]
19. Vampa, G.; McDonald, C.R.; Orlando, G.; Klug, D.D.; Corkum, P.B.; Brabec, T. Theoretical Analysis of High-Harmonic Generation in Solids. *Phys. Rev. Lett.* **2014**, *113*, 073901. [CrossRef]
20. Wu, M.; Ghimire, S.; Reis, D.A.; Schafer, K.J.; Gaarde, M.B. High-harmonic generation from Bloch electrons in solids. *Phys. Rev. A* **2015**, *91*, 043839. [CrossRef]
21. Kruchinin, S.Y.; Krausz, F.; Yakovlev, V.S. Colloquium: Strong-field phenomena in periodic systems. *Rev. Mod. Phys.* **2018**, *90*, 021002. [CrossRef]
22. Shao, C.; Lu, H.; Zhang, X.; Yu, C.; Tohyama, T.; Lu, R. High-Harmonic Generation Approaching the Quantum Critical Point of Strongly Correlated Systems. *Phys. Rev. Lett.* **2022**, *128*, 047401. [CrossRef] [PubMed]
23. McDonald, C.R.; Vampa, G.; Corkum, P.B.; Brabec, T. Intense-Laser Solid State Physics: Unraveling the Difference between Semiconductors and Dielectrics. *Phys. Rev. Lett.* **2017**, *118*, 173601. [CrossRef] [PubMed]
24. Vampa, G.; Hammond, T.J.; Thiré, N.; Schmidt, B.E.; Légaré, F.; McDonald, C.R.; Brabec, T.; Klug, D.D.; Corkum, P.B. All-Optical Reconstruction of Crystal Band Structure. *Phys. Rev. Lett.* **2015**, *115*, 193603. [CrossRef]
25. Luu, T.T.; Wörner, H.J. Measurement of the Berry curvature of solids using high-harmonic spectroscopy. *Nat. Commun.* **2018**, *9*, 916. [CrossRef]
26. Yu, C.; Jiang, S.; Wu, T.; Yuan, G.; Peng, Y.; Jin, C.; Lu, R. Higher harmonic generation from bilayer nanostructures assisted by electron backscattering. *Phys. Rev. B* **2020**, *102*, 241407. PRB, [CrossRef]
27. You, Y.S.; Reis, D.; Ghimire, S. Anisotropic high-harmonic generation in bulk crystals. *Nat. Phys.* **2017**, *13*, 345–349. [CrossRef]
28. Ndabashimiye, G.; Ghimire, S.; Wu, M.; Browne, D.A.; Schafer, K.J.; Gaarde, M.B.; Reis, D.A. Solid-state harmonics beyond the atomic limit. *Nature* **2016**, *534*, 520–523. [CrossRef]
29. Yoshikawa, N.; Tamaya, T.; Tanaka, K. High-harmonic generation in graphene enhanced by elliptically polarized light excitation. *Science* **2017**, *356*, 736–738. [CrossRef]
30. Vampa, G.; Brabec, T. Merge of high harmonic generation from gases and solids and its implications for attosecond science. *J. Phys. B At. Mol. Opt. Phys.* **2017**, *50*, 083001. [CrossRef]

31. Vampa, G.; McDonald, C.; Fraser, A.; Brabec, T. High-Harmonic Generation in Solids: Bridging the Gap Between Attosecond Science and Condensed Matter Physics. *IEEE J. Sel. Top. Quantum Electron.* **2015**, *21*, 8700110. doi: 10.1109/JSTQE.2015.24-02636. [CrossRef]
32. Ghimire, S.; Reis, D.A. High-harmonic generation from solids. *Nat. Phys.* **2019**, *15*, 10–16. [CrossRef]
33. Gruzdev, V.E. Photoionization rate in wide band-gap crystals. *Phys. Rev. B* **2007**, *75*, 205106. doi: 10.1103/PhysRevB.75. 205106. [CrossRef]
34. Zhokhov, P.A.; Zheltikov, A.M. Field-Cycle-Resolved Photoionization in Solids. *Phys. Rev. Lett.* **2014**, *113*, 133903. [CrossRef]
35. Sato, S.A.; Lucchini, M.; Volkov, M.; Schlaepfer, F.; Gallmann, L.; Keller, U.; Rubio, A. Role of intraband transitions in photocarrier generation. *Phys. Rev. B* **2018**, *98*, 035202. [CrossRef]
36. Almalki, S.; Parks, A.M.; Brabec, T.; McDonald, C.R. Nanoengineering of strong field processes in solids. *J. Phys. B At. Mol. Opt. Phys.* **2018**, *51*, 084001. [CrossRef]
37. Wismer, M.S.; Kruchinin, S.Y.; Ciappina, M.; Stockman, M.I.; Yakovlev, V.S. Strong-Field Resonant Dynamics in Semiconductors. *Phys. Rev. Lett.* **2016**, *116*, 197401. [CrossRef]
38. Schlaepfer, F.; Lucchini, M.; Sato, S.A.; Volkov, M.; Kasmi, L.; Hartmann, N.; Rubio, A.; Gallmann, L.; Keller, U. Attosecond optical-field-enhanced carrier injection into the GaAs conduction band. *Nat. Phys.* **2018**, *14*, 560–564. [CrossRef]
39. Tancogne-Dejean, N.; Rubio, A. Atomic-like high-harmonic generation from two-dimensional materials. *Sci. Adv.* **2018**, *4*, eaao5207. [CrossRef]
40. Song, X.; Zuo, R.; Yang, S.; Li, P.; Meier, T.; Yang, W. Attosecond temporal confinement of interband excitation by intraband motion. *Opt. Express* **2019**, *27*, 2225–2234. [CrossRef]
41. Li, L.; Lan, P.; Zhu, X.; Huang, T.; Zhang, Q.; Lein, M.; Lu, P. Reciprocal-Space-Trajectory Perspective on High-Harmonic Generation in Solids. *Phys. Rev. Lett.* **2019**, *122*, 193901. [CrossRef] [PubMed]
42. Du, T.Y. Control of high-order harmonic emission in solids via the tailored intraband current. *Phys. Rev. A* **2021**, *104*, 063110. [CrossRef]
43. Yu, C.; Iravani, H.; Madsen, L.B. Crystal-momentum-resolved contributions to multiple plateaus of high-order harmonic generation from band-gap materials. *Phys. Rev. A* **2020**, *102*, 033105. [CrossRef]
44. Navarrete, F.; Ciappina, M.F.; Thumm, U. Multi-channel contributions to infrared-driven high-harmonic generation in solids. *J. Phys. Conf. Ser.* **2020**, *1412*, 082006. [CrossRef]
45. Liu, J.Q.; Bian, X.B. Effect of electron-electron interactions on high-order harmonic generation in crystals. *Phys. Rev. B* **2020**, *102*, 174302. [CrossRef]
46. Navarrete, F.; Ciappina, M.F.; Thumm, U. Crystal-momentum-resolved contributions to high-order harmonic generation in solids. *Phys. Rev. A* **2019**, *100*, 033405. [CrossRef]
47. McDonald, C.R.; Vampa, G.; Corkum, P.B.; Brabec, T. Interband Bloch oscillation mechanism for high-harmonic generation in semiconductor crystals. *Phys. Rev. A* **2015**, *92*, 033845. [CrossRef]
48. Vampa, G.; McDonald, C.R.; Orlando, G.; Corkum, P.B.; Brabec, T. Semiclassical analysis of high harmonic generation in bulk crystals. *Phys. Rev. B* **2015**, *91*, 064302. [CrossRef]
49. Zhang, X.; Li, J.; Zhou, Z.; Yue, S.; Du, H.; Fu, L.; Luo, H.G. Ellipticity dependence transition induced by dynamical Bloch oscillations. *Phys. Rev. B* **2019**, *99*, 014304. [CrossRef]
50. Qiao, Y.; Huo, Y.Q.; Jiang, S.C.; Yang, Y.J.; Chen, J.G. All-optical reconstruction of three-band transition dipole moments by the crystal harmonic spectrum from a two-color laser pulse. *Opt. Express* **2022**, *30*, 9971–9982. [CrossRef]
51. He, Y.L.; Guo, J.; Gao, F.Y.; Yang, Z.J.; Zhang, S.Q.; Liu, X.S. Interference between harmonics of different crystal momentum channels in solid high-order harmonic generation. *Phys. Rev. A* **2021**, *104*, 013104. [CrossRef]
52. Du, M.; Liu, C.; Zheng, Y.; Zeng, Z.; Li, R. Attosecond transient-absorption spectroscopy in one-dimensional periodic crystals. *Phys. Rev. A* **2019**, *100*, 043840. [CrossRef]
53. Floss, I.; Lemell, C.; Wachter, G.; Smejkal, V.; Sato, S.A.; Tong, X.M.; Yabana, K.; Burgdörfer, J. Ab initio multiscale simulation of high-order harmonic generation in solids. *Phys. Rev. A* **2018**, *97*, 011401. [CrossRef]
54. Bloch, F. Über die Quantenmechanik der Elektronen in Kristallgittern. *Z. Phys.* **1929**, *52*, 555–600. doi: 10.1007/BF0133-9455. [CrossRef]
55. Shao, T.J.; Lü, L.J.; Liu, J.Q.; Bian, X.B. Quantum path interferences and selection in interband solid high-order harmonic generation in MgO crystals. *Phys. Rev. A* **2020**, *101*, 053421. [CrossRef]
56. Du, T.Y.; Tang, D.; Bian, X.B. Subcycle interference in high-order harmonic generation from solids. *Phys. Rev. A* **2018**, *98*, 063416. [CrossRef]